IVYSPRING INTERNATIONAL PUBLISHER

Theranostics

2019; 9(14): 4168-4181. doi: 10.7150/thno.34390

Research Paper

Gadolinium-Chelated Conjugated Polymer-Based Nanotheranostics for Photoacoustic/Magnetic Resonance/NIR-II Fluorescence Imaging-Guided Cancer Photothermal Therapy

Xiaoming Hu[1], Yufu Tang[1], Yuxuan Hu[2], Feng Lu[1], Xiaomei Lu[3], Yuqi Wang[2], Jie Li[1], Yuanyuan Li[1], Yu Ji[1], Wenjun Wang[4], Deju Ye[2], Quli Fan[1]✉ and Wei Huang[1,3,5]

1. Key Laboratory for Organic Electronics and Information Displays (KLOEID) & Institute of Advanced Materials (IAM), Jiangsu National Synergetic Innovation Center for Advanced Materials (SICAM), Nanjing University of Posts & Telecommunications, Nanjing 210023, China.
2. State Key Laboratory of Analytical Chemistry for Life Science, School of Chemistry and Chemical Engineering, Nanjing University, Nanjing, 210093, China
3. Key Laboratory of Flexible Electronics (KLOFE) & Institute of Advanced Materials (IAM), Jiangsu National Synergetic Innovation Center for Advanced Materials (SICAM), Nanjing Tech University (NanjingTech), Nanjing 211816, China
4. Key Lab of Optical Communication Science and Technology of Shandong Province & School of Physics Science and Information Engineering, Liaocheng University, Liaocheng 252059, China
5. Shaanxi Institute of Flexible Electronics (SIFE), Northwestern Polytechnical University (NPU), Xi'an 710072, China.

✉ Corresponding author: E-mail: iamqlfan@njupt.edu.cn

Received: 2019.02.25; Accepted: 2019.04.08; Published: 2019.05.31

Abstract

Our exploiting versatile multimodal theranostic agent aims to integrate the complementary superiorities of photoacoustic imaging (PAI), second near-infrared (NIR-II, 1000-1700) fluorescence and T_1-weighted magnetic resonance imaging (MRI) with an ultimate objective of perfecting cancer diagnosis, thus improving cancer therapy efficacy. Herein, we engineered and prepared a water-soluble gadolinium-chelated conjugated polymer-based theranostic nanomedicine (PFTQ-PEG-Gd NPs) for in vivo tri-mode PA/MR/NIR-II imaging-guided tumor photothermal therapy (PTT).

Methods: We firstly constructed a semiconducting polymer composed of low-bandgap donor-acceptor (D-A) which afforded the strong NIR absorption for PAI/PTT and long fluorescence emission to NIR-II region for in vivo imaging. Then, the remaining carboxyl groups of the polymeric NPs could effectively chelate with Gd^{3+} ions for MRI. The in vitro characteristics of the PFTQ-PEG-Gd NPs were studied and the in vivo multimode imaging as well as anti-tumor efficacy of the NPs was evaluated using 4T1 tumor-bearing mice.

Results: The obtained theranostic agent showed excellent chemical and optical stability as well as low biotoxicity. After 24 h of systemic administration using PQTF-PEG-Gd NPs, the tumor sites of living mice exhibited obvious enhancement in PA, NIR-II fluorescence and positive MR signal intensities. Better still, a conspicuous tumor growth restraint was detected under NIR light irradiation after administration of PQTF-PEG-Gd NPs, indicating the efficient photothermal potency of the nano-agent.

Conclusion: we triumphantly designed and synthesized a novel and omnipotent semiconducting polymer nanoparticles-based theranostic platform for PAI, NIR-II fluorescence imaging as well as positive MRI-guided tumor PTT in living mice. We expect that such a novel organic nano-platform manifests a great promise for high spatial resolution and deep penetration cancer theranostics.

Key words: conjugated polymer, second near-infrared fluorescence imaging, photoacoustic imaging, magnetic resonance imaging, photothermal therapy

Introduction

The development of phototheranostic agents has provided a new insight on cancer and disease research, as well as becoming one of the hotspots in biomedical applications over the past decades, which

was attributing to the incomparable superiorities of integrating real-time diagnosis and in situ phototherapeutic potencies within a single platform [1, 2]. Amidst numerous light-activated diagnostic/therapeutic platforms, deep-tissue optical imaging cooperated with photothermal therapy (PTT) has caught more sights mainly because they are capable of precisely acquiring information of tumor location, effectively facilitate tumor ablation, and scarcely damage healthy tissue [3-6]. As a recent development, fluorescence imaging in the second near-infrared region (NIR-II, 1000-1700 nm) shows unparalleled preponderance for the visualization of histology and pathology with better spatial resolution and deeper tissue penetration than that in the conventional near-infrared window (650-900 nm), mainly benefiting from the lower photo scattering, attenuated autofluorescence and reduced tissue absorption [7-10]. Thus far, some developed fluorophores such as rare-earth-doped materials [11, 12], carbon nanotubes [13-15], quantum dots [16-18], organic small molecules [19-24] and conjugated polymer [25, 26] have presented good performance and superiority for in vivo imaging in the NIR-II region. However, the single function of them and the long-term toxicity misgivings of inorganic materials dramatically limited their further applications [27]. Of note, these NIR-II agents featured with strong NIR absorption can also function as photoacoustic (PA) agents for PA imaging (PAI) and PTT [28, 29]. Thus, developing novel PA/NIR-II imaging-guided cancer PTT theranostic agents based organic materials for intravital applications possesses great significance and positive effect on the field of biomedicine.

With the aid of PA/NIR-II imaging agents, the dual-mode contrast agents possess the capacity for providing high-sensitivity molecular information and fine-resolution morphological structure, but restricted anatomical information [28, 30]. Therefore, integrating with other imaging techniques to preferably acquire synergistic information and complementary superiorities exhibits incomparable advantages for accurately diagnosing cancers and diseases. Magnetic resonance imaging (MRI), a dominant and reliable diagnostic technique for clinical application can provide preeminent physiological and anatomical resolution [31-33]. In order to improve the sensitivity and imaging quality of MRI, contrast agents are consequently conducted. Current MRI contrast agents include T_1-weighted agents generating positive signals and T_2-weighted agents generating negative signals [34]. The magnetic susceptibility artifacts and negative contrast effect of T_2-weighted agents are significant deficiencies in MRI mainly because the resulting dark signals using T_2 agents are frequently confused with the signals from calcification or metal deposits, bleeding, and the obtained susceptibility artifacts misinterpret the background image [35]. Hence, the T_1-weighted contrast agents are generally considered as the preferable imaging agents and play a dominated role in the past decades [36]. As a result, by combining PAI, NIR-II imaging, T_1-weighted MRI and PTT potencies in a single nano-platform, such a nanostructure based-theranostic agent has presented extraordinary preponderance for greatly accurate cancer diagnostic and efficient treatment.

Conjugated polymer nanoparticles (CPNs) have been recently explored to serve as PA and fluorescence imaging agents owning to their excellent optical properties of strong NIR absorption and emission [37-44]. Moreover, due to their optical properties coming from large π-π delocalized frameworks, CPNs commonly have more superior optical-stability compared to small-molecule dyes [45]. More recently, a great increasing number of studies have applied CPNs for in vivo imaging applications as well as cancer theranostics [46-51]. However, reports of the combine of PAI/MRI/NIR-II imaging with PTT performance based CPN are still extremely paucity. Hence, it urges us to expand the library of CPN-based multifunctional integration, which will significantly promote the development of theranostic nanomedicines for biological application.

Herein, we designed and engineered an efficient theranostic nanoagent (PFTQ-PEG-Gd NPs) based on semiconducting conjugated framework and gadolinium ion to realize the deep tissue penetration of enhanced MRI and the fine spatial resolution as well as high signal-to-noise ratio of PAI/NIR-II fluorescence imaging-guided cancer PTT activated by a NIR laser irradiation (Scheme 1). In the system, the conjugated polymer had a semiconducting backbone composed of low-bandgap donor-acceptor (D-A) which possessed strong NIR absorption for PAI/PTT and long fluorescence emission to NIR-II region for biological imaging. In addition, the plentiful COOH groups of the molecular structure are able to afford the conjugated position for introduction of poly(ethylene glycol) (PEG) chains to endow the polymer with excellent water solubility and prolonged circulation time in living mice. Due to the typical amphiphilic molecular structure, the acquired conjugated polymer can be straightly dispersed in aqueous medium and self-assemble into stable nanostructure (PFTQ-PEG NPs). Besides, the remaining carboxyl groups of the polymeric NPs were able to effectively chelate with Gd^{3+} ions for MRI. Noteworthily, the magnetic relativity of the obtained PFTQ-PEG-Gd NPs exhibited a great improvement, owing to the efficient combination performance

between gadolinium ions with the macromolecules, which decelerated their rotational motion and provided more efficient relaxation [36]. The acquired polymeric NPs with a wide absorption region ranging from the visible to NIR window (600-900) and maximum emission wavelength at 1056 nm, possessed an average particle size of ~ 105 nm and showed excellent chemical and optical stability. After systemic administration of the PFTQ-PEG-Gd NPs, the neoplastic mice showed high resolution imaging of blood vessels of the whole body and the tumor areas were obviously lighted up, accompanied by the bright NIR-II imaging, high T_1 relaxivity in MRI and strong PA signal. Better still, the PFTQ-PEG-Gd NPs further served as a powerful photothermal agent to effectively destroy primary tumor. All of these made the NPs can be acted as an efficient theranostic agent for deep-tissue and high-resolution multimode intravital imaging-guided photothermal tumor inhibition.

Results and Discussion

Preparation and Characterization of PFTQ-PEG-Gd NPs

The push-pull approach or donor-acceptor (D-A) system, in which the electron-deficient and electron-rich units are alternatively connected along the molecular framework, shows great superiority for engineering low-bandgap organic conjugated molecules [52]. In our study, we engineered a semiconducting conjugated polymer based on D-A system by utilizing thiadiazoloquinoxaline (TQ) and fluorene (F) as the acceptor and donor, respectively. Firstly, the semiconducting conjugated backbone (PFTQ) was obtained through a grafting-on method. TQ and F derivatives (Scheme S1) were copolymerized through Suzuki reaction to endow the product with near-infrared (NIR) absorption and fluorescence emission to long wavelengths. Then, trifluoroacetic acid can react with the PFTQ polymer molecule to achieve abundant carboxyl groups in order to provide feasible opportunity for the introduction of poly(ethylene glycol) (PEG) chains (Mw = 5000). The triumphant Suzuki polycondensation reaction and conjugation of PEG were characterized by ^{1}H NMR spectra (Figure S1-4), gel permeation chromatography (GPC) (Figure S5 & Table S1) and absorption spectra. The average molecular weight (Mn) of PFTQ and PFTQ-PEG polymer were ~ 40 kDa and ~ 80 kDa, respectively. GPC results manifested that approximately 8 PEG segments are effectively grafted to the macromolecular structure. Then, we recorded the lowest unoccupied molecular orbital (LUMO) and highest occupied molecular orbital (HOMO) of the polymer framework through cyclic voltammograms in dichloromethane. As shown in Figure S6, the LUMO and HOMO are -3.89 and -5.45 eV, respectively. The low electronic band gap (1.56 eV) of the polymer possesses the superiorities for emitting long-wavelength photons [19]. Besides, to endow PFTQ-PEG with magnetic relaxivity performance, the concentrated gadolinium-ion solution was added into PFTQ-PEG aqueous solution, affording the ultimate multifunctional product, PFTQ-PEG-Gd NPs.

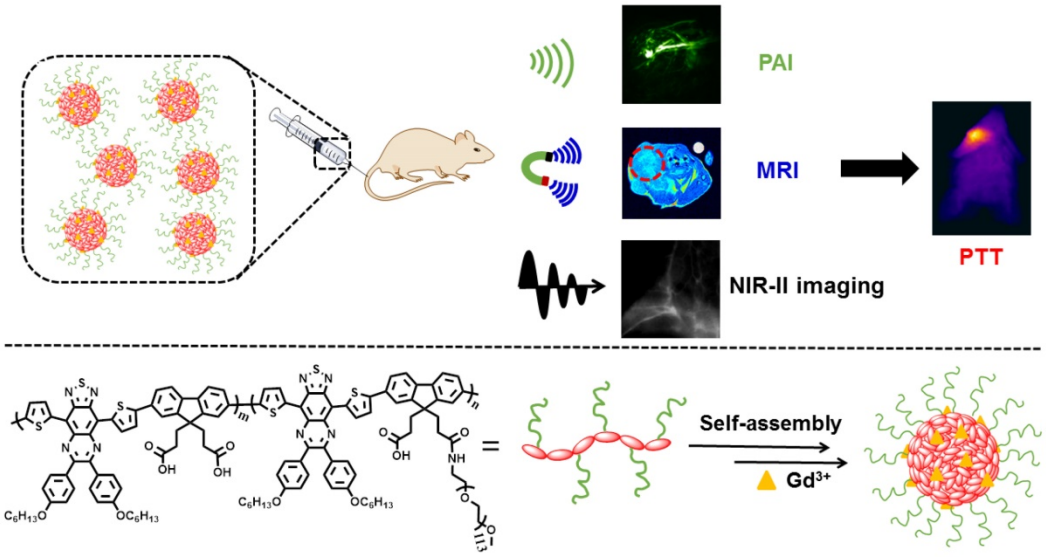

Scheme 1. Schematic Description of the Deep-Tissue and High-Resolution Multimodality Imaging-Guided Cancer Photothermal Therapy in Vivo Using PFTQ-PEG-Gd NPs.

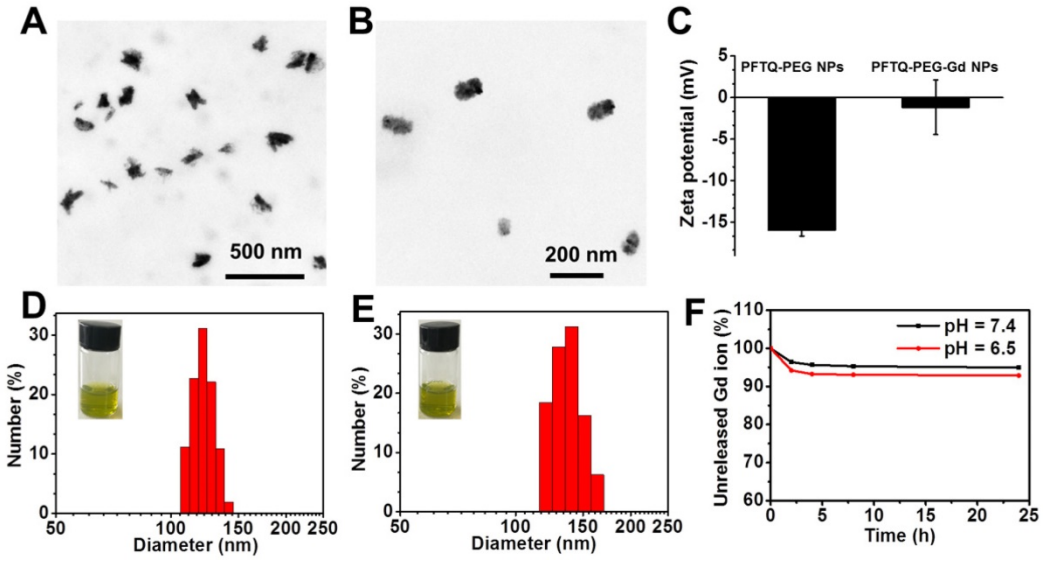

Figure 1. Basic characterization of PFTQ-PEG-Gd NPs and PFTQ-PEG NPs. Representative TEM images of (A) PFTQ-PEG NPs and (B) PFTQ-PEG-Gd NPs. (C) Zeta potentials of PFTQ-PEG-Gd NPs and PFTQ-PEG NPs. Hydrodynamic size distribution graphs of (D) PFTQ-PEG NPs, (E) PFTQ-PEG-Gd NPs and photographs of them in PBS (100 μg mL^{-1}, pH 7.4). (F) The Gd-chelated stability evaluation of PFTQ-PEG-Gd NPs cultivating in different PBS (pH 6.5 and 7.4).

In view of the amphiphilic performance, PFTQ-PEG could be straightly dispersed in water phase, spontaneously assembled into NPs and appeared a yellow green color (Figure 1D). Figure 1A-B and 1D-E described the size changes of PFTQ-PEG NPs that before and after chelating gadolinium ions. As shown, transmission electron microscopy (TEM) image viewed that PFTQ-PEG NPs possessed a homogeneous particle size of 95 ± 4.6 nm (Figure 1A). PFTQ-PEG NPs appeared a splendid dispersity in aqueous solution and dynamic light scattering (DLS) spectra clarified the mean particle diameter of PFTQ-PEG NPs was 123 ± 2.8 nm (Figure 1D). Owing to the conjugation of PEG segments and their unfolded state in watery solution, the particle sizes measured under DLS were bigger than that under TEM images. In addition, after chelating Gd^{3+} ions, the tailor-made PFTQ-PEG-Gd NPs owned a hydrodynamic size of 138.4 ± 3.1 nm (Figure 1E). As shown in the TEM image, the NPs possessed a homogeneous average diameter of ~ 105 nm (Figure 1B). Compared with PFTQ-PEG NPs, the increased particle size of PFTQ-PEG-Gd NPs might ascribe the formed aggregation inside NPs because of the strong chelating action of carboxyl group in PFTQ-PEG NPs toward Gd^{3+} ions. Besides, the increased zeta potential of the PFTQ-PEG-Gd NPs from -10 mV to +0.8 mV (Figure 1C) compared with PFTQ-PEG NPs, further indicated the successful chelation of carboxyl groups within PFTQ-PEG NPs toward gadolinium ions, which was also confirmed by the elemental mapping (Figure S7). Furthermore, the optical properties of PFTQ-PEG-Gd NPs were studied through recording the absorption and fluorescence spectra in aqueous solution and chloroform (Figure 2A and Figure S12). As shown, PFTQ-PEG-Gd NPs possessed an NIR absorption spectrum with a maximum crest at 760 nm and fluorescence emission in the NIR-II window with peak at 1056 nm (Figure 2A) in aqueous solution, hinting a large Stokes shift of approximately 300 nm. The quantum yield (QY) of PFTQ-PEG-Gd NPs was determined to be 0.38%, adopting IR-1061 as a reference (with a reported QY = 1.7%, Figure S10) [53, 54]. In addition, gadolinium ion made no difference to the optical characters of the as-prepared nanostructure after collecting and analyzing the fluorescence and absorption spectra of PFTQ-PEG-Gd NPs and PFTQ-PEG NPs (Figure S11).

The favorable stability of an imaging agent is of great indispensable for in vivo bioimaging. Gadolinium-chelating stability evaluation of PFTQ-PEG-Gd NPs was performed in varying cultivation PBS (pH = 6.5 and 7.4). Figure 1F showed less than 8% of Gd^{3+} ions escaped from the nanostructure in PBS (pH = 6.5) and approximately 95% of Gd^{3+} ions remained within the NPs in PBS (pH = 7.4) after 1 day of incubation, which indicated the first-class stability of the Gd-chelating polymeric NPs and demonstrated incomparable advantages for MRI in vivo. We further monitored the particle size of PFTQ-PEG-Gd NPs in serum after cultivating different points in time. The little changes of the hydrodynamic diameter in serum greatly certified the excellent physiological stability of PFTQ-PEG-Gd NPs (Figure S8). Compared with the smaller size (123 nm) of PFTQ-PEG NPs, the remained size of PFTQ-PEG-Gd NPs in serum also demonstrated that limited Gd^{3+} escaped from serum, proving the good

Gd-chelating stability. Then, we conducted the optical-stability of PFTQ-PEG-Gd NPs along with the indocyanine green (ICG) NPs through acquiring their absorption spectra after a continuous 808 nm (1 W cm^{-2}) laser exposure for a period of time. ICG NPs was acquired by enveloping the commercial ICG dye with amphiphilic DSPE-$mPEG_{2000}$. As shown in Figure 2D, the PFTQ-PEG-Gd NPs showed almost unchanged absorption after 30 min laser cultivation, whereas the peak absorption of ICG NPs gradually decreased and nearly fell to zero under the 30 min laser exposure. Besides, Figure 2C also showed without distinct decay in fluorescence emission intensity of the NPs when suspended in serum, PBS and deionized water after successional irradiation exposure for 30 min. The outstanding optical stability of PFTQ-PEG-Gd NPs was stemmed from the stable π-conjugated polymer backbones, which have repeatedly been demonstrated to be more invulnerable than the conventional small-molecule dyes [55, 56]. In short, the superior physiological, chemical and optical stability of the as-prepared PFTQ-PEG-Gd NPs greatly prompted it for further molecular imaging and bioapplications in vivo.

We further evaluated the capacity of PFTQ-PEG-Gd NPs as a fluorescence contrast agent in the NIR-II window, and the fluorescence signals of PFTQ-PEG-Gd NPs were investigated under 1064 nm LP filters, where 808 nm served as the excitation wavelength was purposely used to equilibrate scattering and absorption to acquire optimal penetration depth for biological imaging. Figure 2B showed PFTQ-PEG-Gd NPs possessed a transparent fluorescence emission signal, while the saline did not emit the signal in NIR-II region, which provided a reliable evidence of the tailor-made agent for intravital NIR-II imaging.

With satisfactory NIR absorption, the in vitro PAI performance of PFTQ-PEG-Gd NPs was first investigated. As shown in Figure 2A, in which the peak absorption of PFTQ-PEG-Gd NPs was 760 nm, we further recorded the in vitro PA images of the NPs with varying contents under an excitation light at 760 nm. Figure 3A-B made clear that the NPs have strong PA signal intensities, which linearly correlated the sample contents. Thus, the tailor-made NPs as resultful PA agents greatly possessed potential for biological imaging.

To probe the potential of our material served as a fine MR contrast agent, the positive MR contrast images were collected with various contents of gadolinium and the magnetic relaxation time (T_1) of the NPs was recorded adopting a 0.5 T MR scanner. The commercial Gd-DTPA contrast agent served as the control group. As shown in Figure 3C, the MR signal intensities of PFTQ-PEG-Gd NPs were proportional to their concentrations. The linear dependence between MR signal and gadolinium content was counted to be 10.95 (termed as magnetic relaxivity r_1 = 10.95 mM^{-1} s^{-1}) as depicted in Figure 3D, which was higher than the widely used Gd-DTPA contrast agents (r_1 = 4.40 mM^{-1} s^{-1}). The emitted more efficient magnetic signal of the agent resulted from the strong chelation among Gd^{3+} ions and the plentiful carboxylate groups, enhancing the hydrogen-bond interaction toward water molecules [57]. Besides, Figure S9 indicated the MR and PA signal intensities of the NPs had fine linear relationship, which demonstrated the platform was highly available for the multimode imaging. All of these results manifested the water-soluble, highly stable and versatile PFTQ-PEG-Gd NPs possessed significant superiority for multimode imaging.

As shown in the aforementioned results, the tailor-made PFTQ-PEG-Gd NPs presented efficient NIR light absorption (Figure 2A), owing the introduction of D-A-type conjugated backbone, which motivated us to explore the photothermal performance of the

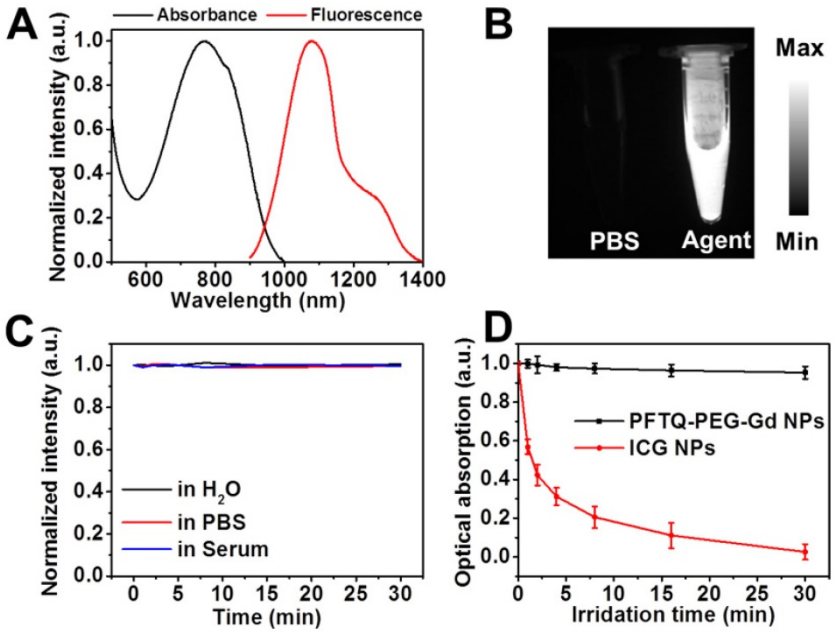

Figure 2. Optical properties of PFTQ-PEG-Gd NPs. (A) Optical spectra of the NPs, manifesting the absorption crest at 760 nm as well as a peak emission at 1056 nm. (B) NIR-II fluorescence images of the NPs (100 μg mL^{-1}) and PBS (pH = 7.4). (C) Photostability assays of the NPs in serum, saline and water via collecting their NIR-II fluorescence signals. (D) Photostability of the NPs (50 μg mL^{-1}) and commercial ICG NPs (50 μg mL^{-1}) via recording their maximum absorption peak (laser exposure: 808 nm, 1 W cm^{-2}).

NPs. As presented in Figure 3F, the photothermal IR images of PFTQ-PEG-Gd NPs with various contents were recorded under an 808 nm (1 W cm^{-2}) light exposure. The PFTQ-PEG-Gd NPs possessed a conspicuous temperature increment, and the NPs exhibited a positive correlation between the increased temperatures with the concentrations of the agent (Figure 3E). By contrast, water did not trigger the obvious temperature increment after the laser irradiation. Besides, the naturally cooling curve was recorded when PFTQ-PEG-Gd NPs reached a stabilized temperature, subsequently the 808 nm light irradiation was switched off (Figure S13). The photothermal conversion efficiency value was computed to be 26% (detailed calculation was presented in Supporting Information), which apparently exhibited more excellent photothermal potency than the widely used gold agents, like gold-nanorods (22%), gold-vesicles (18%) and gold-nanoshells (13%) [58]. The efficient photothermal potency of PFTQ-PEG-Gd NPs provided a theoretical foundation for in vivo PTT.

In Vitro Cytocompatibility and Photothermal Efficacy

In consideration of the preeminent stability and intrinsic photothermal property, we further evaluated the cytocompatibility and extracorporeal photothermal performance of PFTQ-PEG-Gd NPs in the NIH-3T3, 4T1 and Hela cells. We used methyl thiazolyl tetrazolium (MTT) assay to probe the cytotoxicity or cytocompatibility of the NPs. As seen in Figure S14, the cells cultivated with PFTQ-PEG-Gd NPs presented a negligible decrease even at the high dose, indicated the fine cytocompatibility. The phase contrast photomicrographs of the cells treated with the PFTQ-PEG-Gd NPs and PBS (Figure S14E-F) exhibited no obvious morphology difference, which accorded with the quantitative assay results (Figure S14D). Notably, the viable cells decreased obviously along with the increasing concentration of PFTQ-PEG-Gd NPs after administration with a continuous laser radiation for 10 min. Besides, the 4T1 cells conducted with only laser irradiation exhibited relatively excellent cell viability (Figure S14C), implying the laser exposure cannot inhibit the cell survival. After administrating with both laser irradiation and PFTQ-PEG-Gd NPs, the cell survival rate decreased distinctly with the increasing of laser irradiation time (Figure S14C), which further verified the efficient PTT potency of the versatile PFTQ-PEG-Gd NPs. In addition, Figure S15-16 demonstrated the nanoplatform possessed an excellent in vitro and in vivo hemo-compatibility, which was of great significance for potential biomedical applications.

In Vivo Multimode Imaging

As the excellent candidate for in vivo PAI, the PFTQ-PEG-Gd NPs were further studied in xenograft 4T1 neoplastic mice. Before intravenous injection of the nano-agent, the tumor site emitted a slight PA contrast at 760 nm on account of the connatural absorption of oxyhemoglobin and deoxyhemoglobin among the NIR window [47, 59]. Since systemic injection of PFTQ-PEG-Gd NPs, the PA signals in

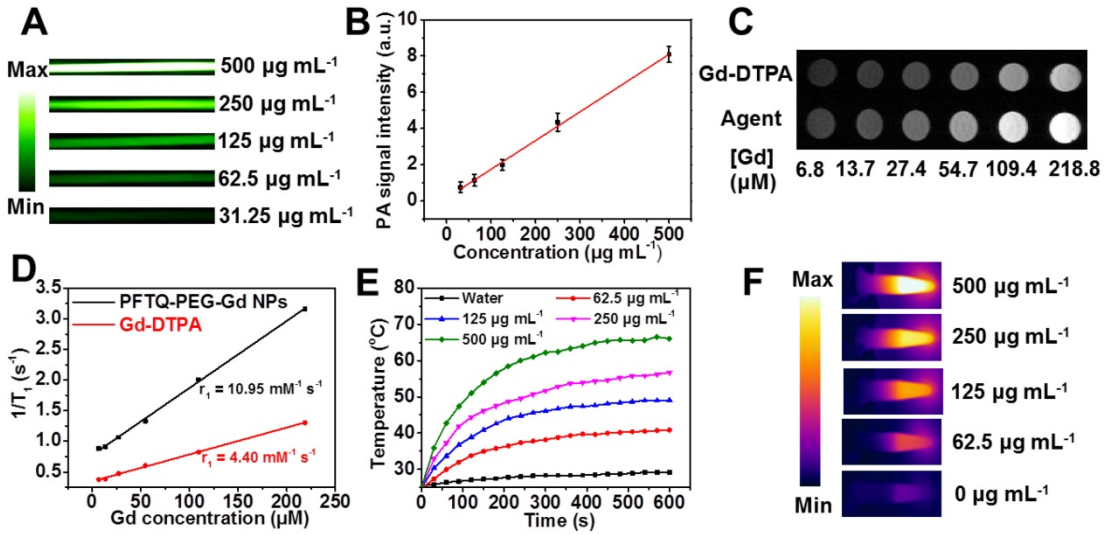

Figure 3. Extracorporeal imaging capacity and photothermal experiments of PFTQ-PEG-Gd NPs. (A) In vitro PA images of the NPs with varying contents ranging from 31.25 to 500 μg mL^{-1}. (B) Linear dependence between the PA signals and concentrations of the NPs (R^2 = 0.996). (C) In vitro positive magnetic contrast images of the NPs (15.6, 31.3, 62.5, 125, 250 and 500 μg mL^{-1}) at varying gadolinium contents (from 6.8 to 218.8 μM), the commercial Gd-DTPA contrast agent (with the equivalent Gd content) served as the control group. (D) Plot of relaxation rates ($1/T_1$) as a function of Gd content of PFTQ-PEG-Gd NPs and Gd-DTPA in saline. (E) Photothermal conversion behavior of PFTQ-PEG-Gd NPs at varying contents (0 - 0.5 mg mL^{-1}) exposed an 808 nm light irradiation. (F) IR thermal images of PFTQ-PEG-Gd NPs at varying contents (0 - 0.5 mg mL^{-1}) under an 808 nm light irradiation.

tumorous locations tardily enhanced as a function of time (Figure 4A), which signified the tumor targeting ability of the NPs via the passive enhanced permeation and retention (EPR) effect. After 24 h post-injection, the PA contrast intensity attained the peak value, which was 4.5 fold stronger than that at pre-injection. In addition, owing to the high resolution of PAI, the 3D PA images could distinctly expose that the PA signals lightened in the regions inside the blood vessels in the deep tumor (Figure 4A). All these proved the PFTQ-PEG-Gd NPs was capable of acting as a resultful imaging agent for intravital high resolution PAI.

Inspired by the fine magnetic potency, the intravital MR contrast performance of PFTQ-PEG-Gd NPs was further investigated on a 4T1 tumorous mouse injected with the agent (150 μL, 1 mg mL^{-1}). Similarly to the results acquired in PAI, the T_1-weighted magnetic signals at the neoplastic locations showed a gradually increased contrast after systemic administration of the agent and achieved the maximum intensity after 24 h post-injection (Figure 4A). Figure 4B exhibited the whole-body MRI of the living mice and the MR signal at 24 h post-injection showed an obvious enhancement compared with that at pre-injection of PFTQ-PEG-Gd NPs. Subsequently, the positive magnetic signals reduced gradually over 24 h post-injection of PFTQ-PEG-Gd NPs, which was roughly accorded with the PAI results (Figure 4C). In addition, compared to the commercial Gd-DTPA contrast agents, the PFTQ-PEG-Gd NPs possessed the prolonged blood circulation, which provided a guarantee for effective tumor accumulation of the NPs (Figure S17).

In consideration of the splendid NIR-II fluorescence emission performance, the 4T1 neoplastic mice were administrated intravenously with the agent (150 μL, 1 mg mL^{-1}) for further evaluating the intravital NIR-II imaging potency of the agent. The real-time intravital NIR-II fluorescence imaging was conducted under a home-built imaging scanner. And the whole mouse was irradiated optically by an 808 nm laser (~ 100 mW cm^{-2}). Of note, the vascular tissue of the whole body could be easily discerned and distinctly "lighted up", which was differentiated from the neighboring background tissues at 2 min post-injection using NIR-II intravital imaging (Figure 5A). Besides, the fluorescence signals of the tumor sites heightened gradually, implying the triumphant tumor accumulation of the NPs as well as subsequently valid fluorescence lighting (Figure 5B-C). The efficient tumor-targeting accumulation could be ascribed to the passive EPR effect of the NPs with size of around 105 nm. As we can see in Figure 5C, NIR-II fluorescence contrast signals within the tumor areas reached a maximum at 1 day post-injection. After that, the fluorescence signals decreased gradually over time, which was attributed to metabolic clearance along with degradation of the NPs under the in vivo biological condition. In

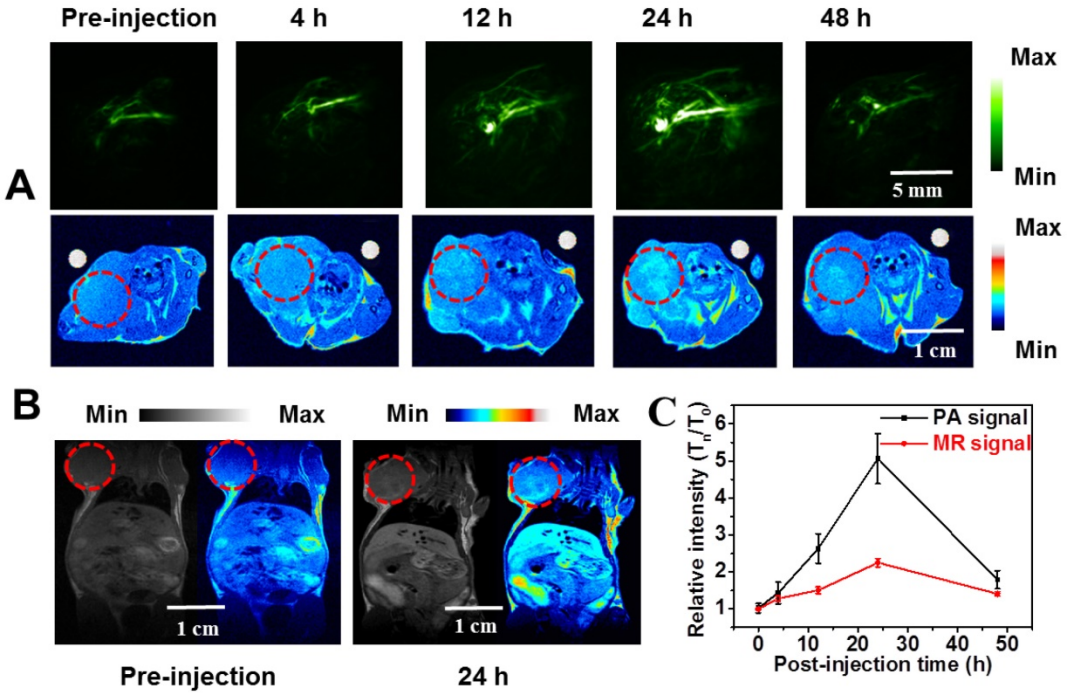

Figure 4. Intravital imaging of 4T1 neoplastic mice. (A) In vivo MRI (below) and PAI (top) of tumorous mice imaged at varying point-in-time after intravenous administration with PFTQ-PEG-Gd NPs. (B) Whole-body MRI images of living mice at 24 h post-injection and pre-injection. (C) PA and MR relative signal values of the tumor regions from neoplastic mice systemically treated with PFTQ-PEG-Gd NPs at different post-injection time points.

addition, after 24 h post-injection of the NPs, the neoplastic mice were performed euthanasia and the primary organs as well as tumor tissue were collected for ex-vivo NIR-II imaging. As depicted in Figure 5D-E, PFTQ-PEG-Gd NPs exhibited a higher distribution in spleen, liver and tumor, while the weak NIR-II fluorescence signals in heart, lung and kidney implied the agent was less distributed within these organs. Thus, the ex-vivo NIR-II contrast imaging demonstrated the tailor-made agent was prevailingly eliminated through the hepatobiliary system. All in all, by feat of PFTQ-PEG-Gd NPs, PAI and NIR-II imaging can provide a deep-penetration and high-resolution superiority for visualizing pathogenic structure and acquiring cancerous information [28, 60]. As a complementarity, the nano-agent is also capable of acting as an MR contrast agent for collecting real-time disease information and probing more precise anatomical date of neoplastic structure in living mice. Therefore, the tailor-made PFTQ-PEG-Gd NPs possesses fine promise to obtain synergetic information and optimal accuracy for high penetration and spatial resolution cancer diagnosis.

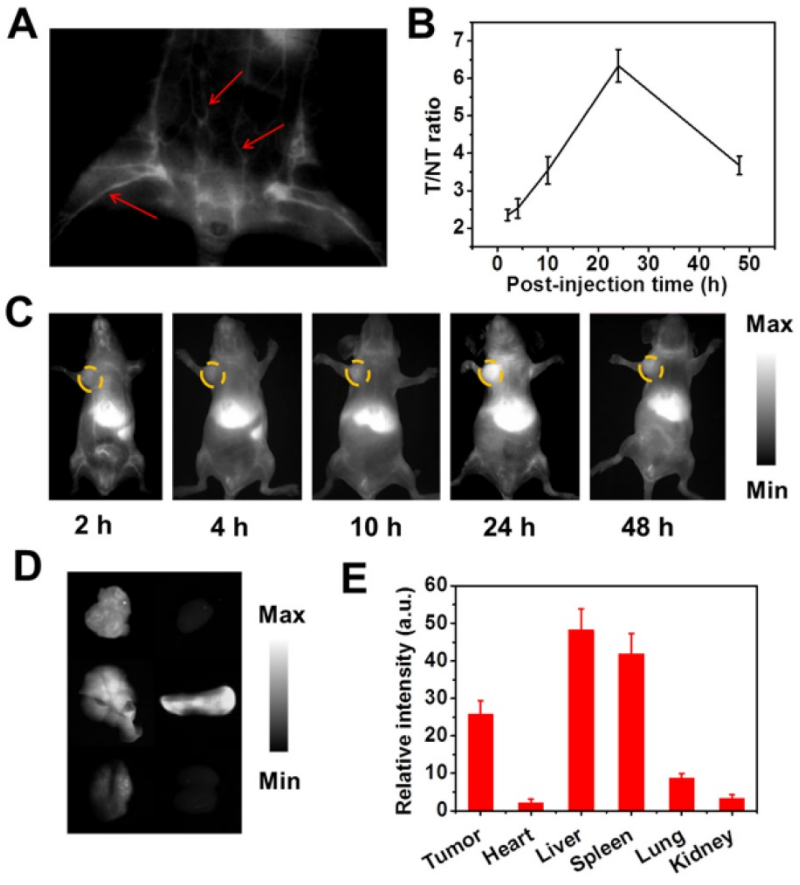

Figure 5. Intravital imaging of 4T1 tumor mice. (A) The NIR-II image of the vascular tissues of the mouse treated with PFTQ-PEG-Gd NPs at 2 min post-injection under 808 nm excitation. The red arrows show the blood vessels. (B) The NIR-II fluorescence of tumor/normal tissue ratio from neoplastic mice systemically treated with PFTQ-PEG-Gd NPs at different post-injection time points. (C) The intravital NIR-II fluorescence contrasts of 4T1 neoplastic mice at varying time points (2, 4, 10, 24, and 48 h) after systemic injection of PFTQ-PEG-Gd NPs. (D) The ex-biodistribution of the agent in neoplastic mice at 24 h post-injection. From left to right and from top to below: tumor, heart, liver, spleen, lung and kidney. (E) Ex-vivo NIR-II fluorescence signal values of some organs from neoplastic mice after 24 h injection with the agent.

In Vivo Tumor Photothermal Therapy Effect

Inspired by the efficacious tumor accumulation and splendid photothermal potency, we further evaluated the PTT effect of PFTQ-PEG-Gd NPs in intravital mice. The 4T1 neoplastic mice were stochastically sectionalized into three groups: (i) PFTQ-PEG-Gd NPs, (ii) saline + laser and (iii) PFTQ-PEG-Gd NPs + laser. Saline (150 μL) and the agent (150 μL, 1 mg mL^{-1}) were administrated into the living mice through systemic injection. On the basis of the obtained results of multimode imaging, in which the agent reached the maximum accumulation within the tumor site at 24 h post-injection, the tumor areas were exposed under an 808 nm (1 W cm^{-2}) laser for 10 min after 24 h post-injection with the agent. The temperature IR images and temperature increase in the tumor areas were imaged under a thermal imaging camera. The temperature in tumor of the living mice treated with the agent + laser speedily increased to above 50 °C within 1 min and almost remained at around 58.5 °C at remaining time points as depicted in Figure 6A-B. The generated hyperthermia is enough competent to kill tumor cells (above 42 °C) [61-63]. The rapidly increased temperature within the tumor site indicated the efficient tumor accumulation of PFTQ-PEG-Gd NPs, further exhibiting the fine passive tumor targeting potency of the agent. By contrast, the control group (ii) treated with saline possessed a feeble temperature increase (from 32.7 to 38.7 °C) under the same light exposure for 10 min, which also suggested the laser exposure itself is unable to destroy the tumor and is sufferable for living mice.

The tumor sizes of different groups were monitored and recorded to availably investigate the tumor PTT therapeutic result. As depicted in Figure 6C, these mice treated with saline + laser exhibited a frustrated tumor restraint and the tumors appeared rapid growth rates, implying that only 808 nm laser exposure is incapable of affecting the tumor growth. Similarly, the tumors performed by only PFTQ-PEG-Gd NPs failed to restrain the tumor development, indicating the agent itself possesses negligible antitumor effect. Exhilaratingly, compare with the two

groups with rapid-growing tumor size, the group (iii) treated with agent + laser presented dramatic tumor growth suppression. The tumor mice in group (iii) showed remarkably smaller tumor volume than the control groups at the same time point, demonstrating the PTT activated by PFTQ-PEG-Gd NPs assisted with NIR laser can indeed suppress tumor growth. In addition, the body weight of each treatment mice was recorded at targeted day and no distinct body weight loss can be viewed in the three treatment group of living mice (Figure 6D), revealing no apparent side effect of all mice and an inappreciable biological toxicity of PFTQ-PEG-Gd NPs. Moreover, at the end of 16 days' treatment, these mice from all treatment groups were conducted euthanasia and some major organs containing lung, kidney, spleen, heart, liver and tumor were collected for the histological hematoxylin and eosin (H&E) staining experiment to clarify the cancer therapeutic effect (Figure 7A). The tumor tissues of group (iii) performed with agent + laser exhibited dramatic apoptosis and necrosis of cancer cells as presented in Figure 7B, implying a triumph of tumor inhibition capability. Additionally, other major organs of all three groups showed no evident tissue necrosis, inflammation or apoptosis, further proving no obvious toxicity of the laser irradiation and agent in intravital animals. All of these results demonstrated that the tailor-made versatile PFTQ-PEG-Gd NPs is capable of serving as a greatly promising theranostic agent for fine-resolution and deep-tissue multimodality imaging-guided cancer PTT.

Conclusions

In summary, we triumphantly designed and synthesized a novel and multifunctional semiconducting polymer nanoparticles based theranostic platform for photoacoustic imaging, NIR-II fluorescence imaging as well as positive magnetic resonance imaging-guided tumor photothermal therapy in living mice. Besides, in view of the numerous superiorities of the nanostructure such as good stability, strong near-infrared (NIR) absorption along with emission wavelength in the NIR-II region and easy modifiability due to the abundant modifiable sites of the polymer framework, we believe the tailor-made PFTQ-PEG-Gd NPs can provide unprecedented chances for engineering a sequence of nano-platforms for intravital biological imaging and cancer theranostics.

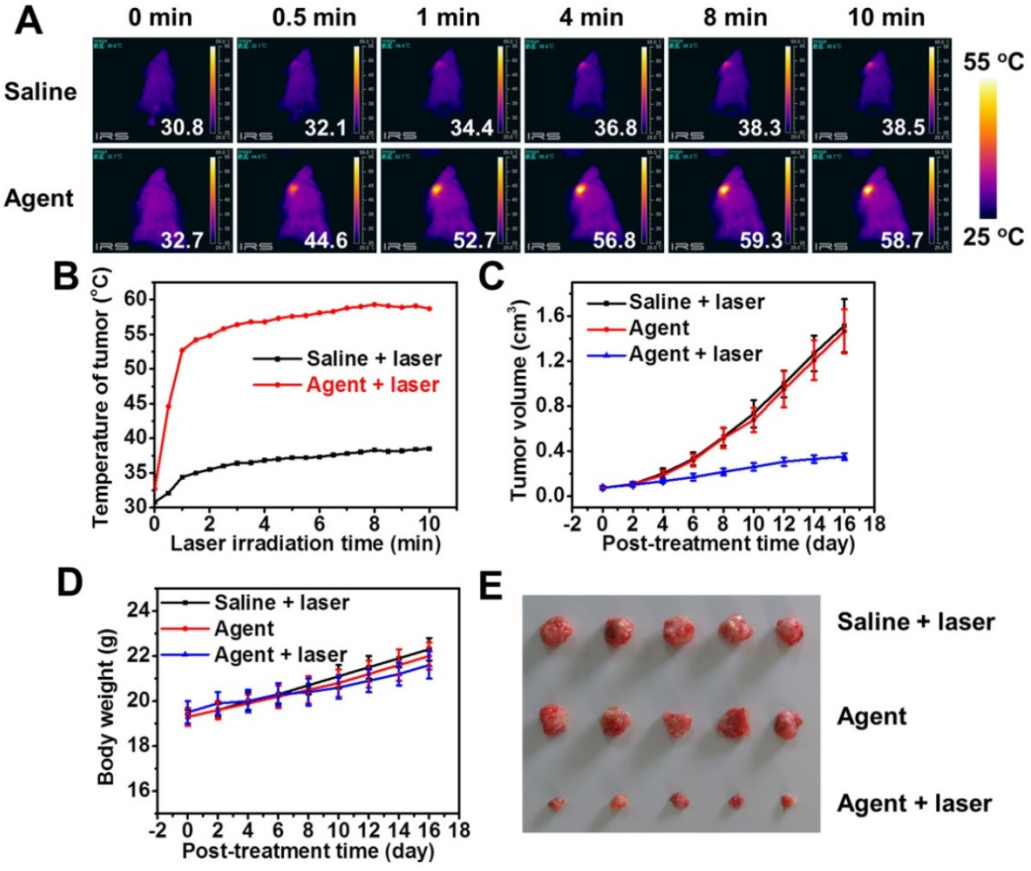

Figure 6. Intravital photothermal tumor therapy. (A) IR thermal images of 4T1 neoplastic mice; (B) Temperature rise on tumor areas of the neoplastic mice injected without or with the agent under an 808 nm laser excitation (1 W cm^{-2}); (C) Tumor volume growth curves of each treatment group of mice; (D) Body weight changes of mice from three treatment groups; (E) Representative photographs of the 4T1 tumors collected from these mice at the end of PTT.

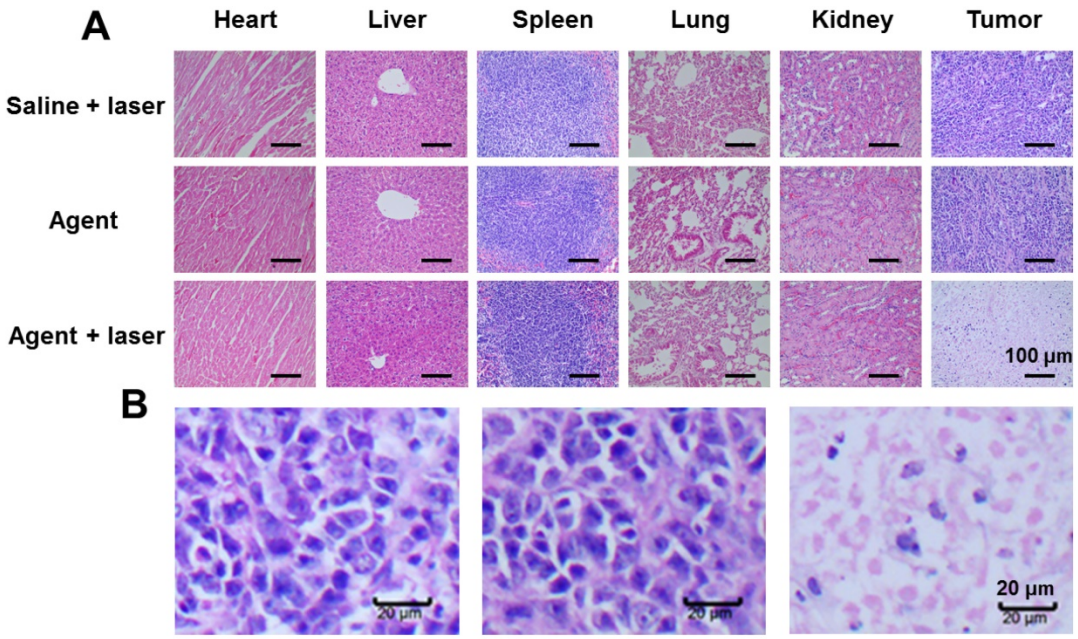

Figure 7. (A) Histological H&E staining of tumor and various organs from the treatment mice. Scale bar: 100 μm. (B) H&E-stained tumors from (left) group "Saline + laser", (middle) group "Agent" and (right) group "Agent + laser". Scale bar: 20 μm.

Experimental Section

Chemicals. 4,9-bis(5-bromothiophen-2-yl)-6,7-bis-(4-(hexyloxy)phenyl)-[1,2,5]thiadi-azolo[3,4-g]quinoxaline (**compound 1**) was purchased from Suna Tech Inc. Di-tert-butyl 3,3'-(2,7-bis(4,4,5,5-tetramethyl-1,3,2-dioxaborolan-2-yl)-9H-fluorene-9,9-diyl)dipropanoate (**compound 2**) was synthesized under the guidance of our previous study [64]. All the chemicals were bought from Sigma-Aldrich, except as otherwise mentioned, and adopted directly.

Synthesis of PFTQ. Compound 1 (69.02 mg, 0.08 mmol), **compound 2** (53.96 mg, 0.08 mmol), K_2CO_3 (110.57 mg, 0.8 mmol), $Pd(PPh_3)_4$ (6.36 mg, 0.0055 mmol) and methyltri°C tylammonium chloride (1.5 mg) dissolving in toluene (3 mL) and water (1.3 mL) were transferred in a Schlenk tube (50 mL) under nitrogen and performed at 100 °C for 36 h. After that, the solvent of the reaction tube was removed under a vacuum pump. The gained solid was extracted using suitable dichloromethane and water for three times. The collected organic solution was further precipitated in excess methanol. The acquired black solid was repeatedly washed by cold methanol and finally dried in a vacuum oven to afford product **3** (PFTQ).

Synthesis of PFTQ-PEG. PFTQ (40 mg) was dispersed in a mixed solution containing trifluoroacetic acid (5 mL) and dichloromethane (10 mL), which appeared a brown color. After stirring over night at room temperature, 50 mL methanol was poured into the reacting solution and the mixed solution appeared green. Next, the solvent was eliminated. The resulting black powder **4** was acquired, and dried in a vacuum oven overnight. Then, product **4** (30 mg), amino poly(ethylene glycol) (NH_2-PEG_{5000}) (50 mg), NHS (25 mg) and EDC·HCl (40 mg) was dispersed in *N*,*N*-dimethylformamide (15 mL) and the solution was stirred at 45 °C for 48 h. After 2 days' reaction, the solvent was wiped out by reduced pressure distillation and deionized water (8 mL) was used to dissolve the mixture under a successional ultrasonic. Subsequently, the aqueous solution was transferred into a dialysis bag (MW 7500 Da) and cultivated in deionized water for 3 days to remove the unreacted NH_2-PEG_{5000}. And the solid of compound **5** (PFTQ-PEG) was obtained in a lyophilizer.

Preparation of Nanoparticles. Firstly, we prepared the PFTQ-PEG NPs via immediately suspending PFTQ-PEG in deionized water under unremitting sonication. Then, PFTQ-PEG-Gd NPs was synthesized as previously depicted, with minor amendment [36]. In detail, the watery solution of PFTQ-PEG NPs (10 mL, 1 mg mL^{-1}) was added with fresh $GdCl_3$ (500 μL, 10 mg mL^{-1}) and incubated at 37 °C for an additional 4 h. To sweep the redundant metal ions and other useless byproducts, a PD-10 column was adopted for purifying the gained complex. The acquired nanoparticles were re-dispersed in saline, concentrated by a 30 kDa centrifugal filter and filtrated passing a millipore filter (0.22 μm) for further in vitro and in vivo assays. For the preparation of indocyanine green (ICG) NPs [52], commercial ICG dye (1 mg) and DSPE-$mPEG_{2000}$ (5 mg) was dissolved in 1-mL tetrahydrofuran (THF).

The obtained solution was swiftly dropped into the mixing solution containing 9-mL water and 1-mL THF under a sequential sonication for two minutes. Then THF was removed by a tepid decompression. The gained NPs were re-dispersed in saline and stored at refrigerator for further experiment.

Instruments and Methods. Transmission electron microscope (TEM) images were collected under a HT7700 TEM apparatus (accelerating voltage: 100kV). A Bruker nuclear magnetic resonance (NMR) spectrometer (^{1}H: 400 MHz, ^{13}C: 100 MHz) was adopted for acquire NMR spectra. The optical absorption of materials was evaluated on a Shimadzu UV-vis-NIR spectrophotometer (UV-3600). The hydrodynamic diameter was administrated on a dynamic light scattering analyzer (Brookhaven, 90 Plus). The cell viability experiments were performed on a microplate reader (BioTek) via methyl thiazolyl tetrazolium (MTT) assays. A commercial photoacoustic imaging (PAI) system (Nexus-128) was used to record all PAI results. All photothermal therapy experiments were conducted under the guidance of a thermal imaging camera (Estonia, FLIR E50).

Cell Culture Assay. The cytocompatibility and photothermal therapy potency of PFTQ-PEG-Gd NPs was conducted via evaluating the 4T1 cell survivability after cultivation in DMEM (Gibco) medium containing different contents of our nanomaterial. Cell survivability evaluation was studied through recording the MTT decrement. These 4T1 cells were sowed in a 96-well plate containing DMEM medium and fetal bovine serum (FBS) and performed at 37 °C for 1 day. Subsequently, these cells were cultured in DMEM medium with a series of concentrations' PFTQ-PEG-Gd NPs for another 6 h and randomly divided into three groups: (i) light irradiation (808 nm, 1 W cm^{-2}) for 10 min, (ii) light irradiation (808 nm, 1 W cm^{-2}) for 5 min and (iii) without laser as a the control group. After that, an accessional 18 h was adopted for breeding the cells. Then, they were transfused with MTT reagent (10 μL, 0.5 mg mL^{-1}) and sequentially cultivated for another 6 h. Finally, we rejected the supernatant and each well plate was added with 200 μL dimethyl sulfoxide (DMSO). The optical absorption at 490 nm, defined as the cellular viability was recorded assisted with a microplate reader. Those undisposed cells' absorption acted as the standard group and was deemed as without cell apoptosis.

Subcutaneous Tumor Models. All animal experiments were performed under the guideline of the Laboratory Animal Center of Jiangsu KeyGEN BioTECH Corp., Ltd and all studies were approved by the Animal Ethics Committee of Model Animal Research Center of Nanjing University. All tumor models were built through subcutaneous injection of 4T1 tumor cells (around 1 × 10^6) in the object region of the living mouse. These tumors freely developed for approximately 4-6 weeks to achieve the volume of ~ 80 mm^3.

In Vitro and in Vivo Photoacoustic Imaging. We assessed the PA signals of as-prepared PFTQ-PEG-Gd NPs with varying concentrations (ranging from 31.25 to 500 μg mL^{-1}) in Fine Bore Polythene Tubing under the guidance of a PA scanner. And excitation wavelength at 760 nm was chosen to acquire the images and date. In vivo PAI assays were performed under the same instrument and operation means. Shortly, the neoplastic mice were systemic administrated with PFTQ-PEG-Gd NPs (150 μL, 1 mg mL^{-1}), narcotized and placed in a dark chamber containing water at 38 °C. Sequences of images at different time point were recorded. A Vevo LAZR PAI System was adopted to reconstruct date. The quantitative value of PA signal was obtained by the identical region-of-interest and the final images were conducted via software OsiriX Lite.

In Vitro and in Vivo Fluorescence Imaging in the Second Near-Infrared Region. The NIR-II fluorescence imaging potency of PFTQ-PEG-Gd NPs was investigated under a home-built fluorescence imaging apparatus (CDD: NIRvana TE 640). The saline was conducted as a control group. Fluorescence images were collected at 900 ~ 1500 nm via applying an 808 nm laser excitation (Ti-Sapphire, laser power: ~ 100 mW cm^{-2}). Similarly, the in vivo NIR-II fluorescence imaging of blood vessels on the whole-body of tumorous mice was performed after systemic administration with our agent (150 μL, 1 mg mL^{-1}). And the in vivo tumor fluorescence images recorded at targeted time point (2, 4, 10, 24, and 48 h) were acquired after injection of the agent.

In Vitro and in Vivo T_1-Weighted Magnetic Resonance Imaging. PFTQ-PEG-Gd NPs with varying contents of Gd ions (218.8, 109.4, 54.7, 27.4, 13.7 and 6.8 μM) were placed in a micro-MRI scanner (0.5 T, NIUMAG, NMI20-015 V-I, TE/TR = 18/120 ms) and the commercial Gd-DTPA contrast agent with the same Gd content was served as a control group. Image analysis was performed by Image J. Besides, the longitudinal relaxivities (r_1) was acquired as the slope of the relaxation rates ($1/T_1$) versus Gd content. Herein, the gadolinium content was quantified using inductively coupled plasma-mass (ICP-MS) spectrometry. The intravital MRI measurement was conducted at a Bruker Micro-MRI (1.5 T). Briefly, 4T1 neoplastic mice, intravenously administrated with PFTQ-PEG-Gd NPs (150 μL, 1 mg mL^{-1}), were placed and imaged at 1.5 T Micro-MRI

(TR/TE =446 ms/15 ms, slice thickness = 1 mm, FOV = 35 mm × 35 mm, matrix 256 × 256). The images at ranging from 0 to 48 h post-injection of the agent were recorded and the image administration was performed through the aforementioned approach using Image J.

In Vitro and in Vivo Photothermal Capacity Evaluation. PFTQ-PEG-Gd NPs with varying content (500, 250, 125, 62.5 μM and deionized water as a control group) was placed and exposed under an 808 nm laser for 10 min (1 W cm^{-2}) to evaluated the in vitro PTT efficacy. As for in vivo PTT assay, after 24 h tail vein administration of sample (PFTQ-PEG-Gd NPs: 150 μL, 1 mg mL^{-1} or saline: 150μL), the neoplastic mice were fixed under laser exposure for 10 min. During all above measurements, the temperature variation was recorded every 30 s through a thermal imaging camera (Estonia, FLIR Systems OU, FLIR E50).

Abbreviations

CPNs: conjugated polymer nanoparticles; DLS: dynamic light scattering; D-A: donor-acceptor; EPR: enhanced permeation and retention; FBS: fetal bovine serum; GPC: gel permeation chromatography; H&E: hematoxylin and eosin; ICG: indocyanine green; MRI: magnetic resonance imaging; MTT: methyl thiazolyl tetrazolium; NIR-II: second near-infrared; PAI: photoacoustic imaging; PEG: poly(ethylene glycol); PBS: phosphate buffered saline; PTT: photothermal therapy; QY: quantum yield; TQ: thiadiazoloquinoxaline; TEM: transmission electron microscopy.

Supplementary Material

Supporting Information. Synthetic route to PFTQ-PEG; GPC date of PFTQ and PFTQ-PEG in THF eluent; ^{1}H-NMR spectra of relevant compound; physiological stability of PFTQ-PEG-Gd NPs; optical properties of PFTQ-PEG NPs and PFTQ-PEG-Gd NPs; the cooling curve of PFTQ-PEG-Gd NPs aqueous solution after laser irradiation; in vitro cytocompatibility and photothermal efficacy; NIR-II fluorescence quantum yield measurement of PFTQ-PEG-Gd NPs; in vitro and in vivo hemocompatibility and in vivo blood elimination kinetics of PFTQ-PEG-Gd NPs.
http://www.thno.org/v09p4168s1.pdf

Acknowledgements

We greatly appreciate the financial support from the National Natural Science Foundation of China (Grant Nos. 21605088, 21674048, and 21574064), the 333 project of Jiangsu province (Grant No. BRA2016379), the Primary Research & Development Plan of Jiangsu Province (Grant No. BE2016770), the Natural Science Foundation of Jiangsu Province (Grant No. BK20160884) and the China Postdoctoral Science Foundation (Grant No. 2017M621792).

Author Contributions

The manuscript was written through contributions of all authors. All authors have given approval to the final version of the manuscript.

Competing Interests

The authors have declared that no competing interest exists.

References

1. Li J, Pu K. Development of organic semiconducting materials for deep-tissue optical imaging, phototherapy and photoactivation. Chem Soc Rev. 2019; 48: 38-71.
2. Cheng L, Wang C, Feng L, Yang K, Liu Z. Functional Nanomaterials for Phototherapies of Cancer. Chem Rev. 2014; 114: 10869-10939.
3. Ma L, Liu Y, Liu L, Jiang A, Mao F, Zhou J, et al. Simultaneous Activation of Short-Wave Infrared (SWIR) Light and Paramagnetism by a Functionalized Shell for High Penetration and Spatial Resolution Theranostics. Adv Funct Mater. 2018; 28: 1705057.
4. Ge J, Jia Q, Liu W, Guo L, Liu Q, Lan M, et al. Red-Emissive Carbon Dots for Fluorescent, Photoacoustic, and Thermal Theranostics in Living Mice. Adv Mater. 2015; 27: 4169−4177.
5. Guo B, Sheng Z, Hu D, Li A, Xu S, Manghnani P, et al. Molecular Engineering of Conjugated Polymers for Biocompatible Organic Nanoparticles with Highly Efficient Photoacoustic and Photothermal Performance in Cancer Theranostics. ACS Nano. 2017; 11: 10124-10134.
6. Hu X, Lu F, Chen L, Tang Y, Hu W, Lu X, et al. Perylene Diimide-Grafted Polymeric Nanoparticles Chelated with Gd^{3+} for Photoacoustic/T_1-Weighted Magnetic Resonance Imaging-Guided Photothermal Therapy. ACS Appl Mater Interfaces. 2017; 9: 30458-30469.
7. Hong G, Antaris AL, Dai H. Near-infrared fluorophores for biomedical imaging. Nat Biomed Eng. 2017; 1: 0010.
8. Yang Q, Ma Z, Wang H, Zhou B, Zhu S, Zhong Y, et al. Rational Design of Molecular Fluorophores for Biological Imaging in the NIR-II Window. Adv Mater. 2017; 29: 1605497.
9. Kenry, Duan Y, Liu B. Recent Advances of Optical Imaging in the Second Near-Infrared Window. Adv Mater. 2018; 30: 1802394.
10. Cai Y, Wei Z, Song C, Tang C, Han W, Dong X. Optical nano-agents in the second near-infrared window for biomedical applications. Chem Soc Rev. 2019; 48: 22-37.
11. Naczynski DJ, Tan MC, Zevon M, Wall B, Kohl J, Kulesa A, et al. Rare-earth-doped biological composites as in vivo shortwave infrared reporters. Nat Commun. 2013; 4: 2199.
12. Wang X, Hu H, Zhang H, Li C, An B, Dai J. Single ultrasmall Mn^{2+}-doped NaNdF4 nanocrystals as multimodal nanoprobes for magnetic resonance and second near-infrared fluorescence imaging. Nano Res. 2017; 11: 1069-1081.
13. Welsher K, Liu Z, Sherlock SP, Robinson JT, Chen Z, Daranciang D, et al. A route to brightly fluorescent carbon nanotubes for near-infrared imaging in mice. Nat Nanotechnol. 2009; 4: 773-780.
14. Antaris AL, Robinson JT, Yaghi OK, Hong G, Diao S, Luong R, et al. Ultra-low doses of chirality sorted (6, 5) carbon nanotubes for simultaneous tumor imaging and photothermal therapy. ACS Nano. 2013; 7: 3644-3652.
15. Welsher K, Sherlock SP, Dai H. Deep-tissue anatomical imaging of mice using carbon nanotube fluorophores in the second near-infrared window. Proc Nati Acad Sci USA. 2011; 108: 8943-8948.
16. Li C, Li F, Zhang Y, Zhang W, Zhang XE, Wang Q. Real-time monitoring surface chemistry-dependent in vivo behaviors of protein nanocages via encapsulating an NIR-II Ag_2S quantum dot. ACS Nano. 2015; 9: 12255-12263.
17. Zhang Y, Hong G, Zhang Y, Chen G, Li F, Dai H, et al. Ag_2S quantum dot: a bright and biocompatible fluorescent nanoprobe in the second near-infrared window. ACS Nano. 2012; 6: 3695-3702.
18. Zhang M, Yue J, Cui R, Ma Z, Wan H, Wang F, et al. Bright quantum dots emitting at approximately 1,600 nm in the NIR-IIb window for deep

tissue fluorescence imaging. Proc Nati Acad Sci USA. 2018; 115: 6590-6595.
19. Antaris AL, Chen H, Cheng K, Sun Y, Hong G, Qu C, et al. A small-molecule dye for NIR-II imaging. Nat Mater. 2016; 15: 235-242.
20. Sun Y, Qu C, Chen H, He M, Tang C, Shou K, et al. Novel benzo-bis(1,2,5-thiadiazole) fluorophores for in vivo NIR-II imaging of cancer. Chem Sci. 2016; 7: 6203-6207.
21. Yang Q, Hu Z, Zhu S, Ma R, Ma H, Ma Z, et al. Donor Engineering for NIR-II Molecular Fluorophores with Enhanced Fluorescent Performance. J Am Chem Soc. 2018; 140: 1715-1724.
22. Sheng Z, Guo B, Hu D, Xu S, Wu W, Liew WH, et al. Bright Aggregation-Induced-Emission Dots for Targeted Synergetic NIR-II Fluorescence and NIR-I Photoacoustic Imaging of Orthotopic Brain Tumors. Adv Mater. 2018; 30: 1800766.
23. Qi J, Sun C, Zebibula A, Zhang H, Kwok RTK, Zhao X, et al. Real-Time and High-Resolution Bioimaging with Bright Aggregation-Induced Emission Dots in Short-Wave Infrared Region. Adv Mater. 2018; 30: 1706856.
24. Wang Q, Xia B, Xu J, Niu X, Cai J, Shen Q, et al. Biocompatible small organic molecule phototheranostics for NIR-II fluorescence/photoacoustic imaging and simultaneous photodynamic/photothermal combination therapy. Mater Chem Front. 2019; DOI: 10.1039/C9QM00036D.
25. Hong G, Zou Y, Antaris AL, Diao S, Wu D, Cheng K, et al. Ultrafast fluorescence imaging in vivo with conjugated polymer fluorophores in the second near-infrared window. Nat Commun. 2014; 5: 4206.
26. Shou K, Tang Y, Chen H, Chen S, Zhang L, Zhang A, et al. Diketopyrrolopyrrole-based semiconducting polymer nanoparticles for in vivo second near-infrared window imaging and image-guided tumor surgery. Chem Sci. 2018; 9: 3105-3110.
27. Li B, Lu L. Zhao M, Lei Z, Zhang F. An Efficient 1064 nm NIR-II Excitation Fluorescent Molecular Dye for Deep-Tissue High-Resolution Dynamic Bioimaging. Angew Chem Int Ed. 2018; 57: 7483-7487.
28. Cheng K, Chen H, Jenkins CH, Zhang G, Zhao W, Zhang Z, et al. Synthesis, Characterization, and Biomedical Applications of a Targeted Dual-Modal Near-Infrared-II Fluorescence and Photoacoustic Imaging Nanoprobe. ACS Nano. 2017; 11: 12276-12291.
29. Alifu N, Zebibula A, Qi J, Zhang H, Sun C, Yu X, et al. Single-Molecular Near-Infrared-II Theranostic Systems: Ultrastable Aggregation-Induced Emission Nanoparticles for Long-Term Tracing and Efficient Photothermal Therapy. ACS Nano. 2018; 12: 11282-11293.
30. Li C, Cao L, Zhang Y, Yi P, Wang M, Tan B, et al. Preoperative Detection and Intraoperative Visualization of Brain Tumors for More Precise Surgery: A New Dual-Modality MRI and NIR Nanoprobe. Small. 2015; 11: 4517-4525.
31. Zhou Z, Qutaish M, Han Z, Schur RM, Liu Y, Wilson DL, et al. MRI detection of breast cancer micrometastases with a fibronectin-targeting contrast agent. Nat Commun. 2015; 6: 7984.
32. Shen Z, Song J, Zhou Z, Yung BC, Aronova MA, Li Y, et al. Dotted Core-Shell Nanoparticles for T_1 -Weighted MRI of Tumors. Adv Mater. 2018; 30: 1803163.
33. Mi P, Kokuryo D, Cabral H, Wu H, Terada Y, Saga T, et al. A pH-activatable nanoparticle with signal-amplification capabilities for non-invasive imaging of tumour malignancy. Nat Nanotechnol. 2016; 11: 724-730.
34. Caravan P. Strategies for increasing the sensitivity of gadolinium based MRI contrast agents. Chem Soc Rev. 2006; 35: 512-523.
35. Na HB, Lee JH, An K, Park YI, Park M, Lee IS, et al. Development of a T1 contrast agent for magnetic resonance imaging using MnO nanoparticles. Angew Chem Int Ed. 2007; 119: 5493-5497.
36. Frangville C, Li Y, Billotey C, Talham DR, Taleb J, Roux P, et al. Assembly of Double-Hydrophilic Block Copolymers Triggered by Gadolinium Ions: New Colloidal MRI Contrast Agents. Nano Lett. 2016; 16: 4069-4073.
37. Feng L, Zhu C, Yuan H, Liu L, Lv F, Wang S. Conjugated Polymer Nanoparticles: Preparation, Properties, Functionalization and Biological Applications. Chem Soc Rev. 2013; 42: 6620-6633.
38. Cui D, Xie C, Pu K. Development of Semiconducting Polymer Nanoparticles for Photoacoustic Imaging. Macromol Rapid Commun. 2017; 38: 1700125.
39. Pu K, Mei J, Jokerst JV, Hong G, Antaris AL, Chattopadhyay N, et al. Diketopyrrolopyrrole-Based Semiconducting Polymer Nanoparticles for In Vivo Photoacoustic Imaging. Adv Mater. 2015; 27: 5184-5190.
40. Chen D, Li Q, Meng Z, Guo L, Tang Y, Liu Z, et al. Bright Polymer Dots Tracking Stem Cell Engraftment and Migration to Injured Mouse Liver. Theranostics. 2017; 7: 1820-1834.
41. Miao Q, Xie C, Zhen X, Lyu Y, Duan H, Liu X, et al. Molecular afterglow imaging with bright, biodegradable polymer nanoparticles. Nat Biotechnol. 2017; 35: 1102-1110.
42. Pu K, Shuhendler AJ, Rao J. Semiconducting polymer nanoprobe for in vivo imaging of reactive oxygen and nitrogen species. Angew Chem Int Ed. 2013; 52: 10325-10329.
43. Cao Z, Feng L, Zhang G, Wang J, Shen S, Li D, et al. Semiconducting polymer-based nanoparticles with strong absorbance in NIR-II window for in vivo photothermal therapy and photoacoustic imaging. Biomaterials. 2018; 155: 103-111.
44. Li D, Zhang G, Xu W, Wang J, Wang Y, Qiu L, et al. Investigating the Effect of Chemical Structure of Semiconducting Polymer Nanoparticle on Photothermal Therapy and Photoacoustic Imaging. Theranostics. 2017; 7: 4029-4040.
45. Yu J, Rong Y, Kuo CT, Zhou XH, Chiu DT. Recent Advances in the Development of Highly Luminescent Semiconducting Polymer Dots and Nanoparticles for Biological Imaging and Medicine. Anal Chem. 2017; 89: 42-56.
46. Pu K, Shuhendler AJ, Jokerst JV, Mei J, Gambhir SS, Bao Z, et al. Semiconducting polymer nanoparticles as photoacoustic molecular imaging probes in living mice. Nat Nanotechnol. 2014; 9: 233-239.
47. Jiang Y, Cui D, Fang Y, Zhen X, Upputuri PK, Pramanik M, et al. Amphiphilic semiconducting polymer as multifunctional nanocarrier for fluorescence/photoacoustic imaging guided chemo-photothermal therapy. Biomaterials. 2017; 145: 168-177.
48. Liu, H. Y.; Wu, P. J.; Kuo, S. Y.; Chen, C. P.; Chang, E. H.; Wu, C. Y.; Chan, Y. H. Quinoxaline-Based Polymer Dots with Ultrabright Red to Near-Infrared Fluorescence for In Vivo Biological Imaging. J. Am. Chem. Soc. 2015; 137: 10420-10429.
49. Zhen, X.; Feng, X.; Xie, C.; Zheng, Y.; Pu, K. Surface engineering of semiconducting polymer nanoparticles for amplified photoacoustic imaging. Biomaterials. 2017; 127: 97-106.
50. Tang Y, Li Y, Lu X, Hu X, Zhao H, Hu W, et al. Bio-Erasable Intermolecular Donor-Acceptor Interaction of Organic Semiconducting Nanoprobes for Activatable NIR-II Fluorescence Imaging. Adv Funct Mater. 2018; 1807376.
51. Zhu H, Fang Y, Zhen X, Wei N, Gao Y, Luo KQ, et al. Multilayered semiconducting polymer nanoparticles with enhanced NIR fluorescence for molecular imaging in cells, zebrafish and mice. Chem Sci. 2016; 7: 5118-5125.
52. Qi J, Fang Y, Kwok RTK, Zhang X, Hu X, Lam JWY, et al. Highly Stable Organic Small Molecular Nanoparticles as an Advanced and Biocompatible Phototheranostic Agent of Tumor in Living Mice. ACS Nano. 2017; 11: 7177-7188.
53. Tao Z, Hong G, Shinji C, Chen C, Diao S, Antaris AL, et al. Biological imaging using nanoparticles of small organic molecules with fluorescence emission at wavelengths longer than 1000 nm. Angew Chem Int Ed. 2013; 52: 13002-13006.
54. Casalboni M, De Matteis F, Prosposito P, Quatela A, Sarcinelli F. Fluorescence efficiency of four infrared polymethine dyes. Chem Phys Lett. 2003; 373: 372-378.
55. Fan Q, Cheng K, Yang Z, Zhang R, Yang M, Hu X, et al. Perylene-diimide-based nanoparticles as highly efficient photoacoustic agents for deep brain tumor imaging in living mice. Adv Mater. 2015; 27: 843-847.
56. Xie C, Zhen X, Lei Q, Ni R, Pu K. Self-Assembly of Semiconducting Polymer Amphiphiles for In Vivo Photoacoustic Imaging. Adv Funct Mater. 2017; 27: 1605397.
57. Zheng XY, Zhao K, Tang J, Wang XY, Li LD, Chen NX, et al. Gd-Dots with Strong Ligand-Water Interaction for Ultrasensitive Magnetic Resonance Renography. ACS Nano. 2017; 11: 3642-3650.
58. Zhang S, Guo W, Wei J, Li C, Liang XJ, Yin M. Terrylenediimide-Based Intrinsic Theranostic Nanomedicines with High Photothermal Conversion Efficiency for Photoacoustic Imaging-Guided Cancer Therapy. ACS Nano. 2017; 11: 3797-3805.
59. Cai Y, Liang P, Tang Q, Yang X, Si W, Huang W, et al. Diketopyrrolopyrrole–triphenylamine organic nanoparticles as multifunctional reagents for photoacoustic imaging-guided photodynamic/photothermal synergistic tumor therapy. ACS Nano. 2017; 11: 1054-1063.
60. Tang Y, Li Y, Hu X, Zhao H, Ji Y, Chen L, et al. "Dual Lock-and-Key"-Controlled Nanoprobes for Ultrahigh Specific Fluorescence Imaging in the Second Near-Infrared Window. Adv Mater. 2018; 1801140.
61. Goldberg SN, Gazelle GS, Mueller PR. Thermal Ablation Therapy for Focal Malignancy: A Unified Approach to Underlying Principles, Techniques, and Diagnostic Imaging Guidance. AJR Am J Roentgenol. 2000; 174: 323-331.
62. Wang S, Zhao J, Yang H, Wu C, Hu F, Chang H, et al. Bottom-up synthesis of WS_2 nanosheets with synchronous surface modification for imaging guided tumor regression. Acta Biomater. 2017; 58: 442-454.

63. Zhao J, Xie P, Ye C, Wu C, Han W, Huang M, et al. Outside-in synthesis of mesoporous silica/molybdenum disulfide nanoparticles for antitumor application. Chem Eng J. 2018; 351: 157-168.
64. Li J, Tian C, Yuan Y, Yang Z, Yin C, Jiang R, et al. A Water-Soluble Conjugated Polymer with Pendant Disulfide Linkages to PEG Chains: A Highly Efficient Ratiometric Probe with Solubility-Induced Fluorescence Conversion for Thiol Detection. Macromolecules. 2015; 48: 1017-1025.